Supplemental Material

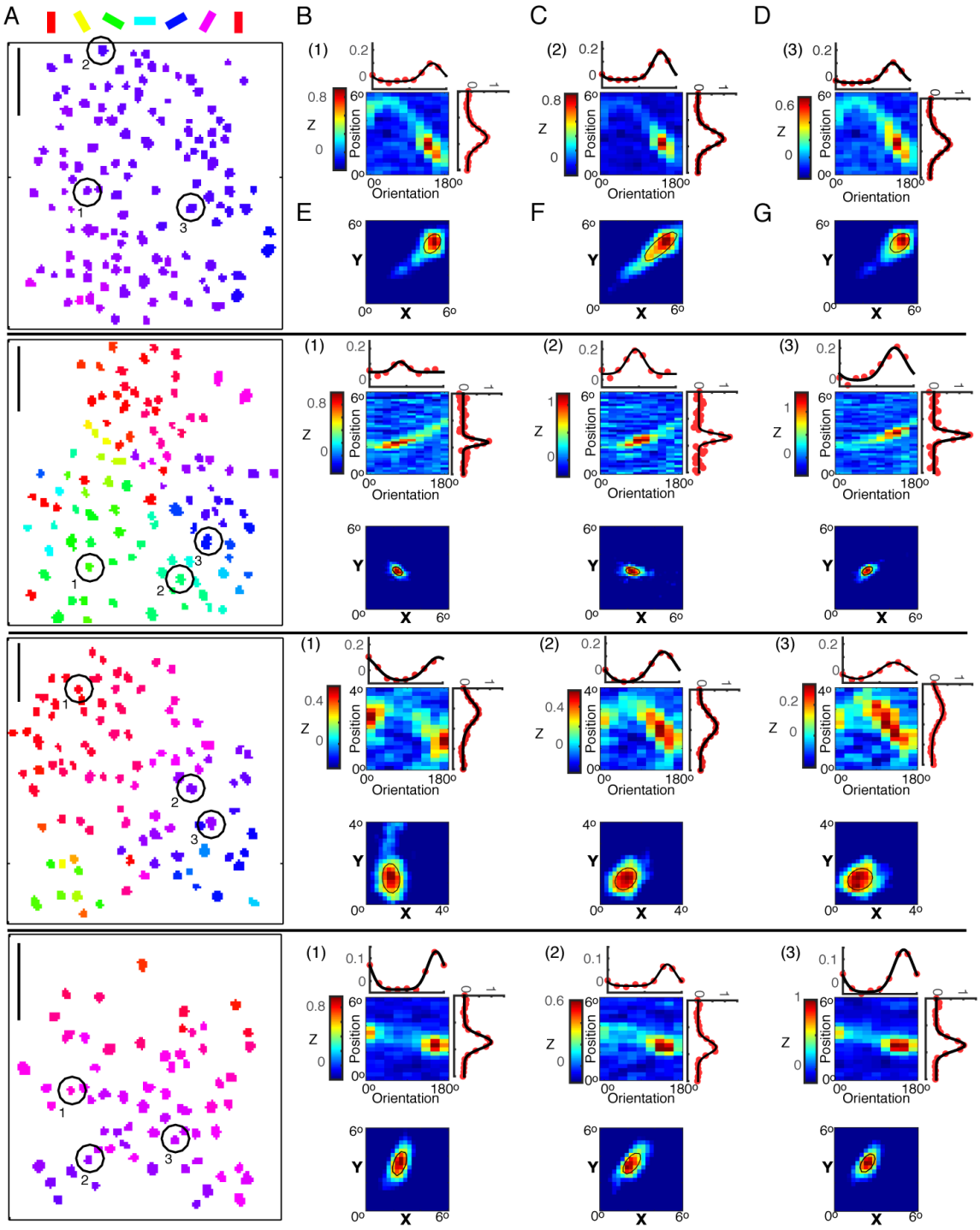

Figure S1, related to Figure 4; Example receptive fields: Three receptive fields from 4 imaging regions. Each of the four rows corresponds to one of the four imaging regions shown in Fig. 4 of the main text. (A) The orientation map, also shown in Fig. 4D, is given here for reference. The three example cells are circled and labeled '1', '2', or '3'. Scale bar at top left is 50 microns. (B) The raw kernel for the example cell labeled '1'. Given after averaging the black and white responses ('position' vs. 'orientation'; e.g. Main Text Fig. 3C). (C) The raw kernel from example cell '2'. (D) The raw kernel from example cell '3'. (E) The corresponding backprojection image ('X' vs. 'Y'; e.g. Fig.3D) to the raw kernel in B. Overlayed on the backprojection image is the contour of the 2D Gaussian fit. (F) Same as E, but for the raw kernel in C. (G) Same as E, but for the raw kernel in D.

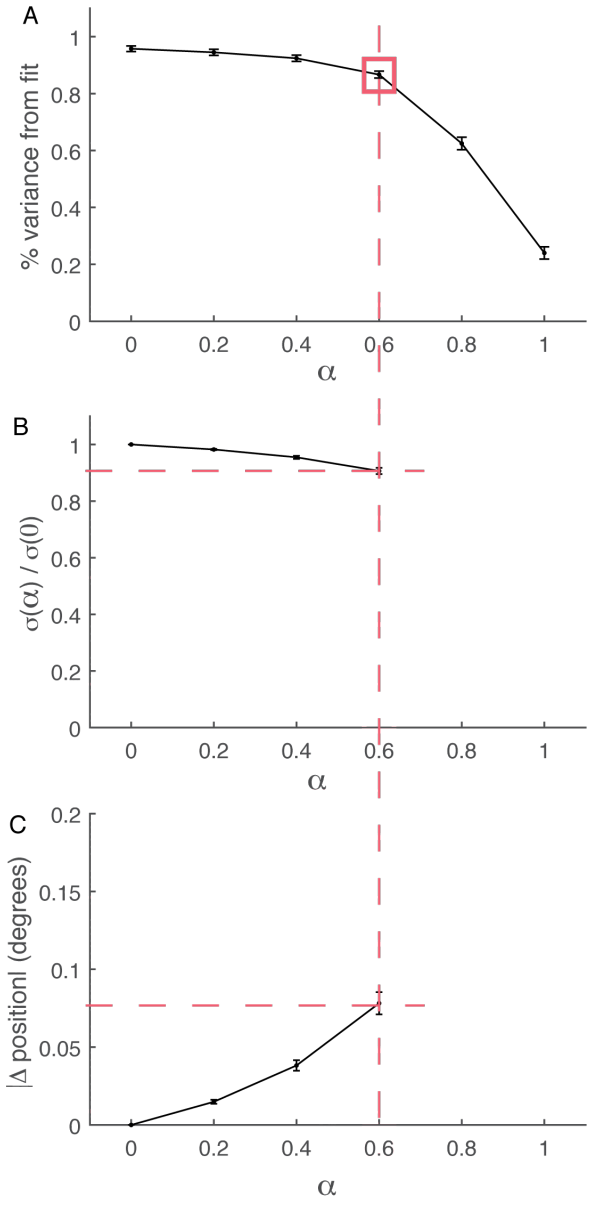

Figure S2, related to Figure 4; Effects of neuropil subtraction on receptive field width and scatter: (A) Dependence of the quality of a Gaussian fit (spatial envelope) on the magnitude of neuropil subtraction. X-axis is the amount of neuropil subtraction; i.e. α in Supp. Eq. 1. Y-axis is the %variance accounted for by the 1D Gaussian fit to the RF along the axis of optimal orientation. The error bars represent the mean and standard error of the entire population of cell bodies in all 6 imaging regions. (B) Dependence of RF

width on the magnitude of neuropil subtraction. X-axis is the same as in (A). Y-axis is the ratio of RF width after subtraction to the RF width before neuropil subtraction. All cells bodies were used. Only values out to $\alpha = 0.6$ are shown because values greater than this are difficult to interpret due to poor Gaussian fits. (C) Change in RF position vs. magnitude of neuropil subtraction. Y-axis is the absolute change, (i.e. $\sqrt{\Delta x^2 + \Delta y^2}$) in RF position after subtracting the neuropil. Only values out to $\alpha = 0.6$ are shown because values greater than this are difficult to interpret due to poor Gaussian fits.

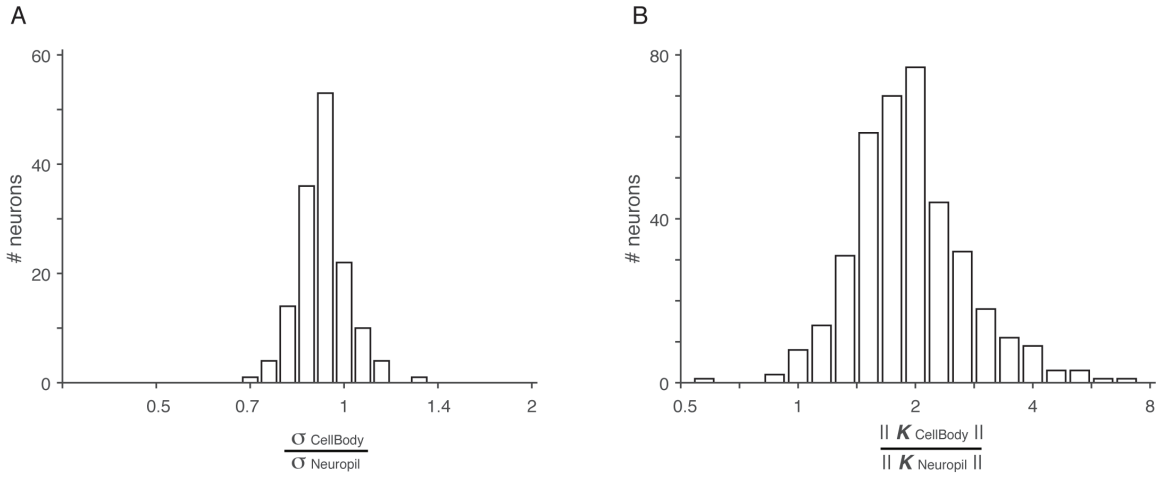

Figure S3, related to Figure 4; Comparing RF width and response magnitude between neuropil and cell-bodies: (a) Distribution comparing size of the cell body RFs to the corresponding neuropil RF. All six imaging regions are included. Each data point is a ratio of σ from the cell body to σ from the corresponding neuropil, both obtained with a Gaussian fit. Median ~ 0.92. (b) Distribution of relative response magnitude between neuropil and corresponding cell bodies. Response magnitude was computed from the norm of the response kernel. All six imaging regions are included. Median ~ 1.9.

Supplemental Experimental Procedures

With bulk-loaded calcium imaging, regions between cell-bodies (i.e. "neuropil") often exhibit a stimulus-locked response. A general concern in two-photon imaging is that the neuropil response bleeds into the signals recorded at the cell bodies (i.e. "neuropil contamination"), predominantly due to the finite imaging resolution along the Z-axis (Kerr and Denk, 2008). In the context of this study, it is important to consider the possible influence of neuropil contamination on RF scatter measurements. If we assume that the neuropil signal represents a superposition of responses from nearby neurons, then the local RF scatter will broaden the RF signal carried by the neuropil. In turn, if there were substantial RF scatter in V1, neuropil contamination would artificially broaden our RFs (measured based on neural responses) and reduce the perceived amount of relative scatter in RF position (Fig. 4C). In our case, it would have to render any scatter virtually undetectable. Support for the mere detectability of RF scatter comes from a qualitative assessment of the orientation tuning independence shown in Figures 4D and E. If substantial RF scatter (Hubel and Wiesel, 1974) were not detectable with OGB two-photon imaging because of the neuropil contamination, then the independence of orientation tuning at pinwheels would also not be detectable. Yet, the data show clear tuning curve separation of >2σ within the same field-of-view (Fig. 4E, rows two and three).

Using off-line processing to remove neuropil contamination from each neuron can be challenging. Ideally, neuropil contamination is removed by isolating spike times from the calcium traces at each cell body, but spike rates in primate V1 are too high to make this feasible with OGB. An alternative solution is to subtract a sample of the surrounding neuropil signal from each cell body. However, this method is difficult to constrain – how much of the neuropil signal does one subtract, and where in the image is the neuropil signal derived? Below, we describe our analysis of neuropil subtraction to assess its impact on the results of receptive field (RF) scatter in Figure 4 and Table 2. The analysis was not designed to "solve" the problem of removing neuropil contamination, but rather to make a conservative estimate of the degree to which neuropil contamination *could* impact our conclusions about RF scatter. In summary, a response kernel was computed for the global neuropil in each imaging region, and then subtracted from the kernels of each cell body. The RF widths and locations were then re-computed as described in the main text (Fig. 3). We found that this procedure had very little effect on RF size and position, thus very little effect on relative RF scatter.

As in the main text, we define the response kernel from a group of pixels as $K(\theta,P)$; the average response amplitude to each orientation (θ) and bar position (P) (Fig. 3). Like prior studies (Bonin et al., 2011; Kerlin et al., 2010), we assume that the *measured* kernel from each cell body ($\boldsymbol{K}_{\text{cellBody}}$) is a weighted sum of two kernels: one from the neuron itself ($\boldsymbol{K}_{\text{neuron}}$) and one from the neuropil ($\boldsymbol{K}_{\text{neuropil}}$).

$$\boldsymbol{K}_{\text{cellBody}} = \boldsymbol{K}_{\text{neuron}} + \alpha\boldsymbol{K}_{\text{neuropil}} \qquad \textit{Supp. Eq. 1}$$

The spatial origin of neuropil contamination is not known. We make the conservative estimate that the neuropil contamination, $\boldsymbol{K}_{\text{neuropil}}$, is the same signal for all cells (i.e. does not vary with $\boldsymbol{K}_{\text{cellBody}}$) and is computed by averaging all pixels of each frame, exclusive to those at cell bodies. If one were to instead use a smaller, arbitrary region centered on each cell (e.g. a doughnut around the cell), $\boldsymbol{K}_{\text{neuropil}}$ would not change much under the current assumption of its origin - the superposition of the local population (e.g. all cells along a columnar penetration). The reason a more local vs. global measure of neuropil would be similar is because V1 RFs are much larger than the change in retinotopy within our fields of view (~250 microns), regardless of the amount of scatter.

We asked the following: What happens to RF width and position as one subtracts variable amounts of $\boldsymbol{K}_{\text{neuropil}}$? More specifically, how does the RF width computed from $\widehat{\boldsymbol{K}}_{\text{neuron}} = \boldsymbol{K}_{\text{cellBody}} - \alpha\boldsymbol{K}_{\text{neuropil}}$ change as a function of α? As in the main text, RF width was computed by fitting a 1D Gaussian to the spatial tuning curve at the optimal orientation (Fig. 3C, dashed line). We note that subtracting kernels is effectively the same as subtracting raw time courses, followed by computing the subsequent kernel, due to the fact that computing each kernel is a linear operation.

We first scaled our two known variables, $\boldsymbol{K}_{\text{cellBody}}$ and $\boldsymbol{K}_{\text{neuropil}}$, to each have a maximum of 1. Next, $\widehat{\boldsymbol{K}}_{\text{neuron}}(\alpha,i) = \boldsymbol{K}_{\text{cellBody}}(i) - \alpha\boldsymbol{K}_{\text{neuropil}}$ was computed for each cell body (i) and a range of coefficient values; α = [0 .2 .6 .8 1.0]. Next, a 1D Gaussian was fit to each $\widehat{\boldsymbol{K}}_{\text{neuron}}(\alpha,i)$ at the peak orientation (Fig. 3C) to give the spatial tuning curve, $\widehat{\boldsymbol{K}}_{\text{neuron}}(\alpha,i|\theta_o)$. As α increased, $\widehat{\boldsymbol{K}}_{\text{neuron}}(\alpha,i|\theta_o)$ began to look less like a

Gaussian and therefore less like the envelope of a V1 neuron's RF. The likeness of $\widehat{\boldsymbol{K}}_{\text{neuron}}(\alpha,i|\theta_o)$ to a Gaussian was quantified using the % variance accounted for by the fit. A plot of %variance vs. α is shown in Figure S2A. Its clear that there is a sharp fall off after $\alpha = 0.6$. That is, neuropil subtraction of $\alpha > 0.6$ leaves mostly noise behind. So, as a conservative estimate of the amount of neuropil contamination, we used $\alpha = 0.6$ to assess the potential impact on measured RF width. Figure S2B plots the RF width from $\widehat{\boldsymbol{K}}_{\text{neuron}}(\alpha,i)$, relative to the width from the original kernel, $\widehat{\boldsymbol{K}}_{\text{neuron}}(0,i)$. Specifically, the mean and standard error of $\sigma(\alpha,i)/\sigma(0,i)$ are shown (σ is from 1D Gaussian fit), for all six imaging regions. There is a shallow drop in RF width as α increases to 0.6. At $\alpha = 0.6$, the RF widths only shrank by ~5%. We also computed the absolute change in RF position at $\alpha = 0.6$, for each cell. The mean change was only 0.07^{o}. These computed values for RF shrinkage and repositioning from the maximum allowable neuropil subtraction are not sufficient to support the possibility of the alternative hypothesis - substantial RF scatter in V1.

The modest 5% change in RF width after neuropil subtraction is supported by Fig. S3A, which compares the width of $\boldsymbol{K}_{\text{cellBody}}(i)$ to the width of $\boldsymbol{K}_{\text{neuropil}}$. The distribution shows that a cell body's RF tends to be marginally narrower than that of the surrounding neuropil (median difference ~ 8%). This observation is consistent with 1) our result that there is minimal scatter in V1 and 2) the notion that a neuropil RF represents the local superposition of the neural population. However, an alternative scenario is that the signals at our cell bodies are completely swamped by the neuropil. Although this seems unlikely based on previous studies with OGB, we also compared the raw signal strength between cell body and neuropil. To compute response magnitude, we took the norm of each kernel, $||\boldsymbol{K}||$. Importantly, unlike the analysis in the main text, the time courses were not Z-scored prior to computing the kernels for this analysis. Instead, only the mean was subtracted in order to capture the raw magnitude of stimulus-triggered deflection. Almost all of the cell bodies yield response amplitudes that are greater than the neuropil (Fig. S3B). The median ratio is near 1.9.

Supplemental References

Bonin, V., Histed, M.H., Yurgenson, S., and Reid, R.C. (2011). Local diversity and fine-scale organization of receptive fields in mouse visual cortex. J. Neurosci. Off. J. Soc. Neurosci. *31*, 18506–18521.

Hubel, D.H., and Wiesel, T.N. (1974). Uniformity of monkey striate cortex: a parallel relationship between field size, scatter, and magnification factor. J. Comp. Neurol. *158*, 295–305.

Kerlin, A.M., Andermann, M.L., Berezovskii, V.K., and Reid, R.C. (2010). Broadly tuned response properties of diverse inhibitory neuron subtypes in mouse visual cortex. Neuron *67*, 858–871.

Kerr, J.N.D., and Denk, W. (2008). Imaging in vivo: watching the brain in action. Nat. Rev. Neurosci. *9*, 195–205.